Electronic Supplementary Material (ESI) for Energy & Environmental Science.
This journal is © The Royal Society of Chemistry 2023

Supporting Information

Terbium-induced cobalt valence-band narrowing boosts electrocatalytic oxygen reduction

Xuan Wang,[#a] Juan Zhang,[#a] Pu Wang,[a] Liangcheng Li,[a] Huiyu Wang,[a] Dongmei Sun,[a] Yafei Li,[a] Yawen Tang,[a] Xue Feng Lu,*[b] Yu Wang,*[a] Gengtao Fu*[a]

[a] Jiangsu Key Laboratory of New Power Batteries, Jiangsu Collaborative Innovation Center of Biomedical Functional Materials, School of Chemistry and Materials Science, Nanjing Normal University, Nanjing 210023, China. E-mail: yu.wang@njnu.edu.cn; gengtaofu@njnu.edu.cn

[b] State Key Laboratory of Photocatalysis on Energy and Environment, College of Chemistry, Fuzhou University, Fuzhou 350108, China. E-mail: luxf@fzu.edu.cn

[#] These authors contributed equally to this work.

Materials and Methods

Chemicals

Melamine ($C_3H_6N_6$), sucrose ($C_{12}H_{22}O_{11}$), cobalt nitrate hexahydrate (Co $(NO_3)_2 \cdot 6H_2O$), and terbium nitrate hexahydrate ($Tb(NO_3)_3 \cdot 6H_2O$) were obtained from Macklin Biochemical Co. (Shanghai, China), Ltd. All reagents and chemicals were used without further purification in this work.

Synthesis of catalysts

In a typical process, 3 g melamine and 2 g sucrose were mixed into 60 mL deionized water and the obtained mixture was further agitated for at least 30 min. Afterward, 1.2 mmol $Co(NO_3)_2 \cdot 6H_2O$ and 0.6 mmol $Tb(NO_3)_3 \cdot 6H_2O$ were introduced into the above mixture solution and were further agitated for at least 2 h to realize the sufficient coordination of Co^{2+} and Tb^{3+}. After the complete coordination, the mixture was transferred into a 100 mL Teflon-lined stainless autoclave and maintained at 200 ℃ for 10 h. After the natural cooling down, the brown precipitate was collected and centrifuged with washing of deionized and ethanol several times. After the treatment of drying, the precursor powder was calcined at 800 ℃ for 3 h under the 10% H_2/Ar atmosphere with the speed of 3 ℃ min^{-1}. The final product was labeled as Co@Tb_2O_3/NC. In comparison, Co/NC and Tb_2O_3/NC were also prepared through a similar procedure except for the addition of Tb^{3+} and Co^{2+} resources respectively.

Physicochemical characterization

The powder X-ray diffraction (XRD) was performed on a Rigaku MiniFlex 600 I diffractometer with Cu Kα radiation of wavelength of 0.15 nm. Raman spectra were collected on a Raman spectrometer (Lab RAM HR800) at the radiation wavelength of 514 nm. The *ex-situ* X-ray photoelectron spectroscopy (XPS) was recorded on a Thermo VG Scientific ESCALAB 250 spectrometer with an Al Kα radiation. The surface area and pore size distribution were detected by the Brunauer-Emmett-Teller (BET) method on a Micromeritics ASAP 2050 instrument in an N_2 atmosphere at 77 K. Transmission electron microscopy (TEM) images and scanning electron microscopy (SEM) were collected on JEOL JSM-2100F TEM/STEM and JEOL JSM7500F at an accelerating high voltage of 200 kV respectively. The energy-dispersive X-ray spectroscopy (EDS) and elemental mapping distribution were obtained from an FEI Tecnai G2 F20 microscope with an accessory built on JEOL JEM2100F. The thermogravimetric analysis (TGA) was recorded over a NetzschSTA449C thermal analyzer with a heating rate of 10 ℃ min^{-1} under the air atmosphere.

Electrochemical Measurements

Electrode preparation

Typically, 5 mg target powder was dispersed into 1000 μL solution composed of 700 μL deionized water, 200 μL ethanol, and 100 μL Nafion under ultrasonic resonance for at least 30 min. Then, 20 μL catalyst ink was dropped onto the glassy carbon rotating ring-disk electrode with a disk area of 0.196 cm^2 to operate as the working electrode. The drying of catalyst ink was in a 40 ℃ constant temperature system.

Electrochemical tests

All the ORR electrochemical tests were operated *via* a typical three-electrode system on CHI 760E electrochemical analyzer (Shanghai Chenghua Co.), where the RRDE was used as the working electrode, carbon electrode as the auxiliary electrode, and a saturated calomel reference electrode protected by Luggin capillary with KCl solution as the reference electrode. In this work, all the measured potentials were calibrated to the reversible hydrogen electrode (RHE) by $E_{RHE} = E_{SCE} + 0.05916*pH + 0.242$, where E_{SCE} is the standard potential of the saturated calomel electrode. The cyclic voltammetry (CV) tests were recorded both in N_2 and O_2-saturated 0.1 M KOH (pH=13). Afterward, the linear sweeping voltammetry (LSV) curves were collected in O_2-saturated 0.1 M KOH electrolyte with the sweeping rate of 5 mV s^{-1} at 25 ℃ under the rotating speed of 1600 rpm. With the different rotating speeds from 400 rpm to 2025 rpm, the effective electron-transfer number (n) of the catalyst sample was measured by the Koutecky-Levich (K-L) equation according to eq (1):

$$\frac{1}{j} = \frac{1}{j_d} + \frac{1}{j_k} = \frac{1}{nFkC_{O_2}} + \frac{1}{0.2nFC_{O_2}D_{O_2}^{\frac{2}{3}}\nu^{-\frac{1}{6}}\omega^{\frac{1}{2}}} \quad (1)$$

where j_d is the diffusion-limited current density, j_k is the kinetic current density, n is the number of electrons transferred per O_2 molecule, F is the Faraday constant (96485 C mol^{-1}), k is the kinetic constant, C_{O_2} is the concentration of O_2 in the bulk electrolyte, D_{O_2} is the diffusion coefficient of O_2 in the electrolyte, ν is the kinematic viscosity of 0.1 M KOH, and ω is the rotating speed of the RRDE. Therefore, the n value can be extracted from the slope of the linear plot of j^{-1} *vs.* $\omega^{-\frac{1}{2}}$. In terms of Tafel slope, the j_k is determined from K-L equation in eq (2):

$$j_k = \frac{j \times j_d}{j_d - j} \quad (2)$$

The percentage of hydrogen peroxide production $\%HO_2^-$ and n based on RRDE can be further calculated by eq (3)-(4):

$$\%HO_2^- = 200\times\frac{i_r}{i_r + N\cdot i_d} \quad (3)$$

$$n = \frac{4\cdot N\cdot i_d}{i_r + N\cdot i_d} \quad (4)$$

where i_r and i_d are the ring and disk current from RRDE curves respectively, and the N is the ring current collection efficiency, which is determined to be 37%. To achieve the chronoamperometric *i-t* curves, the catalyst sample loaded on RRDE was performed at 0.75 V *vs.* RHE in O_2-saturated 0.1 M KOH electrolyte under continuous 1600 rpm for 10 h. And afterward, the obtained final product after *i-t* test was carefully accumulated for further characterization.

The potential-dependent electrochemical impedance spectroscopy (EIS) was collected over a wide potential range from 1.21 V to 0.51 V vs. RHE without rotating speed, where the frequency shifted from 10^6 Hz to 0.5 Hz.

The electrochemical double-layer capacitance (C_{dl}) was obtained at the non-faradic potential range through eq (5):

$$C_{dl} = \frac{\Delta j}{\Delta v} \quad (5)$$

where j is the current density measured from CV and v is the scan rate.

Quasi-operando XPS measurements

The quasi-operando XPS characterization was performed in Thermo ESCALAB 250Xi X-ray photoelectron spectroscope. In detail, the whole X-ray cell consists of preparation chamber, a reaction chamber, and an analysis chamber. For ORR progress, as the same with electrochemical test, the RRDE was used in O_2-saturated 0.1 M KOH solution. The rotating speed of RRDE was set to be 1600 rpm. The KCl-saturated calomel reference electrode was placed in the Luggin capillary and a carbon rod acted as a counter electrode. Strictly, the calomel electrode was placed on a side junction of the electrochemical cell to inhibit the contamination of Cl^-. Before the ORR characterization, the catalyst electrode was placed into a reaction chamber (0.1 M KOH electrolyte), which was deaerated by Ar and saturated with O_2. Afterwards, the reactor was vacuumized till the pressure was lower than 10^{-8} torr and was transferred into the analysis chamber for further steps. During the whole electrochemical test, the potential downshifted from 1.0 V *vs.* RHE to 0.2 V *vs.* RHE with alternate 0.1 V gap. At the initial potential of 1.0 V *vs.* RHE, the catalyst electrode was polarized for 5 min until the XPS

signals were stable. The potential sweep rate was set to be 5 mV s^{-1}. All the elemental binding energy was calibrated relative to the C 1s peak energy of 284.6 eV.

Zn-air battery tests

Liquid Zn-air battery

The liquid Zn-air battery tests were operated in a homemade cell, where the anode was composed of a polished Zn foil. The cathode electrocatalyst ink was prepared through mixing 10 mg electrocatalysts with 250 μL dispersion solution. The dispersion solution was made up of 100 μL deionized water, 100 μL ethanol, and 50 μL Nafion. The air cathode mainly consists of a porous carbon paper with a gas diffusion layer (GDL). The catalyst ink was first dropped onto the porous carbon paper and dried at the constant 40 ℃. The alkaline electrolyte used in liquid Zn-air battery was the mixture of 6 M KOH and 0.2 M $ZnCl_2$. The Lan CT2001A system was used to operate the charge/discharge test such as discharge under various densities, long-cycle stability, and specific capacity, where each charge/discharge period was set to be 10 min. The battery tests for open circuit voltage and power density were realized on CHI 760 E electrochemical analyzer system.

Solid-state Zn-air battery

The assembly of flexible solid-state Zn-air battery is comprised of a polished Zn plate, a piece of flexible nickel foam with loaded catalyst of 1.0 mg cm^{-2}, and a piece of electrolyte gel. The electrolyte gel should be first prepared. In detail, 10 mL mixed solution is composed of 0.5 M ZnO and 11.25 M KOH; after the ultrasonic dispersion, the transparent solution can be obtained. Afterward, 0.1 g N, N'- methylene bisacrylamide was added into the above solution to lead the ultrasonic dispersion. After at least 40 min dispersion, 1 g acrylic acid (AA) was added into the mixture solution and was under ultrasonic for more than 10 min. Then, the solution was transferred into a glassware and was further added dropwise with 0.3 M $(NH_4)_2S_2O_8$ to make the solution polymerize into electrolyte gel. Finally, the flexible solid-state Zn-air battery was constructed with air electrode, Zn plate electrode, and the electrolyte gel, where the two side of electrolyte gel was sealed by pieces of 3 M acrylic tape. Similar to the tests in liquid Zn-air battery, the open-circuit potential and the power density were operated *via* CHI 760 E electrochemical analyzer system. The discharge processes under various current densities, the bend-relaxation test, and the long-term stability test were operated at Lan CT2001A system.

Theoretical calculations

All the spin-polarized density functional theory (DFT) calculations were performed *via* Vienna *ab initio* Simulation Package (VASP).[1, 2] The Perdew-Burke-Ernzerhof (PBE) functional under general gradient approximation (GGA) method was selected.[3] The projector augmented-wave (PAW) method was used to

describe the interactions between ions and electrons.[4] The cut-off energy for the plane-wave basis was set to be 450 eV, which is accompanied with Gaussian smearing of 0.05 eV close to the Fermi level. In detail, O $2s^2 2p^4$, Co $3d^8 4s^1$, and Tb $5s^2 5p^6 4f^9 6s^2$ states were treated as valence electrons. For geometric optimization, the force and energy convergence criteria were chosen to be 0.03 eV/Å and 10^{-5} eV respectively. The vacuum layer chose 15 Å to avoid the self-interactions between the periodically repeated slabs. The Monkhorst-Pack *k*-points integration was set to be 4 × 4 × 4 in the first Brillouin-zone integration.[5] For slab model, the Monkhorst-Pack k-points integration was 2 × 2 × 1. To describe the weak interaction, the van deer Waals correction (DFT-D) was set to be DFT-D3 proposed by Grimme et al.[6, 7] To treat the strongly-localized interaction derived from Co-d and Tb-f electrons, the Hubbard model (DFT+U) was supplied by Dudarev et al,[8] where the effective Hubbard U_{eff} value (*U-J*) adopted 2 eV and 6 eV for Co and Tb respectively according to previous researches.[9, 10] The exposed surface Tb_2O_3 for catalytic mechanism investigation in DFT calculations was (111) surface.

To describe the oxygen reduction reaction (ORR) process in DFT simulation, the computational hydrogen electrode (CHE) model provided by Nørskov[11] was used. In CHE model, the standard electrode process of $H^+ + e^- \rightarrow 0.5H_2(g)$ is treated with the equal free energy between $H^+ + e^-$ and 0.5 H_2 (g) at standard hydrogen electrode (SHE) condition (U_{SHE}=0, pH=0), which the former is hard to be described by DFT calculation. At the condition of T=298.15 K and p=0.035 bar, the free energy of H_2O (l) is equal to H_2O (g), so we can treat $G(H_2O, l) = G(H_2O, g)$ for further electrocatalytic calculation in DFT. By referring to the process of $2H_2$ (g)+ O_2 (g)$\rightarrow 2H_2O$ (l), the free energy of O_2 can be obtained as $G(O_2) = 2G(H_2O, l) - 2G(H_2) + 4.92$ eV because that the triplet ground state of O_2 is difficult to be determined accurately within GGA-DFT. For every oxygen intermediate, the free energy can be calculated as $G = E + ZPE - TS$, where E is the total energy determined from DFT, ZPE is the zero-point vibration energy, T is the temperature, and S is the entropy. The detailed ORR mechanism follows as:

$$O_2 + H^+ + e^- + * \rightarrow *OOH \quad (\Delta G_1)$$

$$*OOH + H^+ + e^- \rightarrow *O + H_2O\ (l) \quad (\Delta G_2)$$

$$*O + H_2O\ (l) + H^+ + e^- \rightarrow *OH + H_2O\ (l) \quad (\Delta G_3)$$

$$*OH + H_2O\ (l) + H^+ + e^- \rightarrow * + 2H_2O\ (l) \quad (\Delta G_3)$$

Correspondingly, the free energy changes of each elementary step are as follows:

$$\Delta G_1 = G(*OOH) - G(O_2) - 0.5G(H_2) - G(*)$$

$$\Delta G_2 = G(*O) + G(H_2O, l) - G(*OOH) - 0.5G(H_2)$$

$$\Delta G_3 = G(*OH) - G(*O) - 0.5G(H_2)$$

$$\Delta G_4 = G(H_2O) + G(*) - G(*O) - 0.5G(H_2)$$

The ZPE is calculated by $\sum_i \frac{1}{2} h\nu_i$, where h is the plank constant and ν_i is the vibrational frequency. The entropy contribution is calculated *via* the following eq (6):

$$TS = \sum_i \frac{h\nu_i}{\exp\left(\frac{h\nu_i}{k_B T}\right) - 1} - k_B T \sum_i ln[1 - \exp\left(-\frac{h\nu_i}{k_B T}\right)] \quad (6)$$

The bias effect on the free energy change of each elementary steps relating with the electron transfer can be treated with $\Delta G(U) = -eU_{SHE}$, where e is the elementary charge transferred.

Note: brief introduction of Newns-Anderson-Grimley model for adsorption process

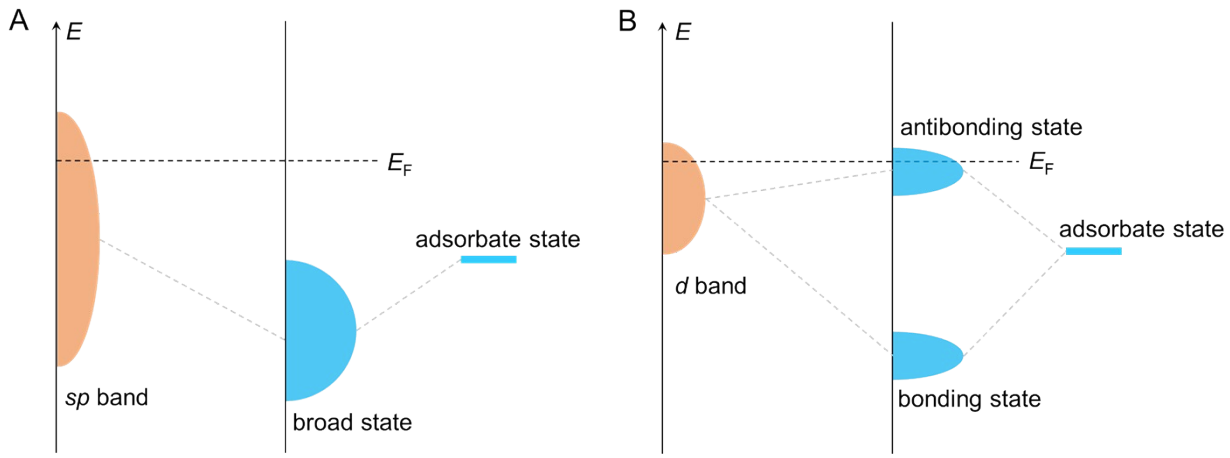

In terms of the relation between band width and the catalytic behavior, the Newns-Anderson-Grimley model provides the standard description. This model demonstrates that hybridization between adsorbates (A) and surface metal site (M) with the broad valence band (such as *sp* band) can create the broadened M-A bonding state (Figure A). Otherwise, for the hybridization between A and M with the narrow band (such as *d* band), the splitting of M-A into bonding and antibonding states occurs (Figure B). Typically, the graphical solution of Newns-Anderson-Grimley model based on the Hilbert transformation of the metal 3*d*-PDOS can approximately describe the different roles of 3*d* band width over catalytic adsorption. The mathematic formula for Hilbert transformation is $\varepsilon = argmax \frac{1}{\pi} P \int_{-\infty}^{+\infty} \frac{\rho(\varepsilon')}{\varepsilon - \varepsilon'} d\varepsilon'$, where P is the principal value of the integral. Such Hilbert transformation can be performed via *scipy.signal.hilbert* within the SCIPY package, the Python code (*www.*

scipy. org). When the band splitting occurs, the occupancy of antibonding states below the Fermi level actually determines the bonding strength for the interaction between metal site and adsorbate. Furthermore, for adsorbate with more valence bands such as *p* states, the orbital coupling between metal site and adsorbate can induce additional π bond beyond the σ bond. Consequently, this model implies that both of the position and band width of metal 3*d* band should be included to determine the bonding strength for chemisorption.

Figures and Tables

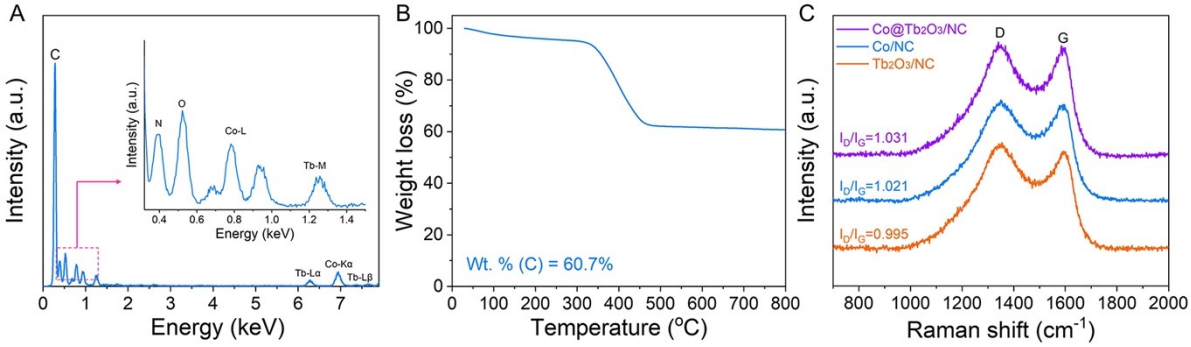

Figure S1. Physical characterizations. (A) The EDX test for elemental detection in Co@Tb_2O_3/NC. (B) TGA plot for Co@Tb_2O_3/NC. (C) Raman spectra for Co@Tb_2O_3/NC, Co/NC, and Tb_2O_3/NC.

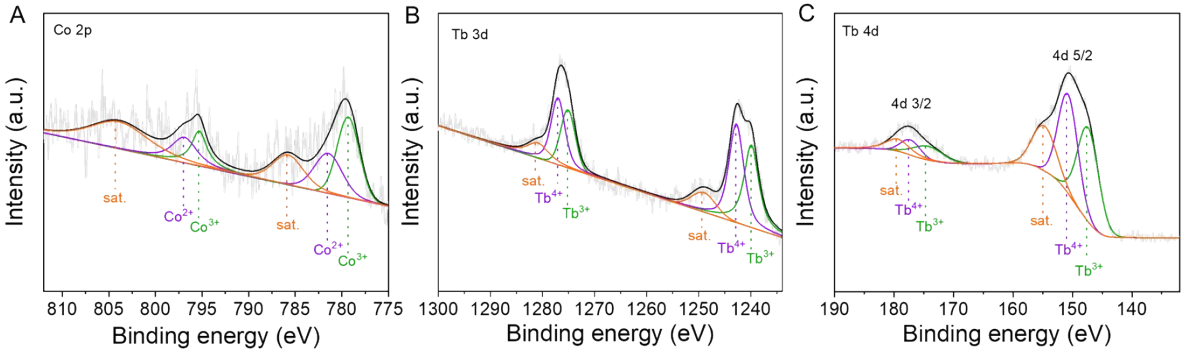

Figure S2. Electronic spectra investigation. (A to C) High-resolution XPS spectra with deconvoluted contribution for Co 2*p*, Tb 3*d*, and Tb 4*d* in Co@Tb_2O_3/NC.

High-resolution Co 2p in Figure S2A reveals the main peak at 779.57 eV and 795.41 eV. The deconvoluted Co^{3+} and Co^{2+} compositions are located at 779.29 eV (Co^{3+}), 795.29 eV (Co^{3+}), 781.58 eV (Co^{2+}), and 797.00 eV (Co^{2+}). Correspondingly, the satellite peaks are in 785.95 eV and 804.41 eV. For high-resolution Tb 3d spectra (Figure S2B), two main peaks at 1242.45 eV and 1276.46 eV are observable. Two main peaks can be further deconvoluted into Tb^{4+} and Tb^{3+} species, which can be attributed to 1242.86 eV (Tb^{4+}), 1277.05 eV (Tb^{4+}), 1239.98 eV (Tb^{3+}), and 1275.18 eV (Tb^{3+}). Two peaks at 1249.47 eV and 1281.38 eV correspond to the satellite peaks. As similar to Tb 3d, high-resolution Tb 4d spectra (Figure S2C) also deliver two main peaks at 150.74 eV and 177.74 eV. The Tb^{4+} contributions in Tb 4d spectra are located at 151.03 eV and 177.51 eV, while Tb^{3+} contributions are at 147.57 eV and 174.94 eV. Two satellite peaks are at 155.07 eV and 179.68 eV.

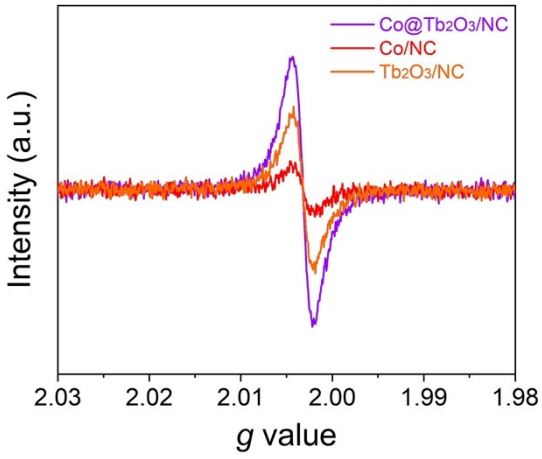

Figure S3. Physical property investigation. EPR plots of $Co@Tb_2O_3/NC$, Co/NC, and Tb_2O_3/NC.

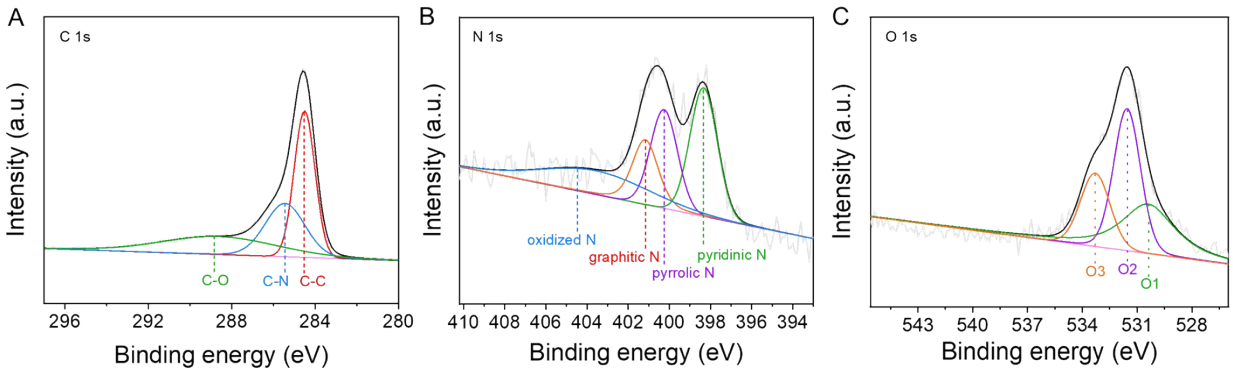

Figure S4. Electronic spectra investigation. (A to C) High-resolution XPS spectra with deconvoluted contribution for C 1s, N 1s, and O 1s in $Co@Tb_2O_3/NC$.

High resolution C 1s spectra in Figure S4A can be deconvoluted into C-C bonds (284.6 eV), C-N bonds (285.49 eV), and C-O bonds (288.87 eV) respectively. For high-resolution N 1s spectra, four peaks can be deconvoluted at 398.35 eV, 400.25 eV, 401.18 eV, and 404.49 eV, corresponding to pyridinic N, pyrrolic N, graphitic N, and oxidized N respectively (Figure S4B). High-resolution O 1s spectra in Figure S4C shows the existence of three contributions at 530.45 eV, 531.54 eV, and 533.34 eV. These contributions are assigned with lattice oxygen (O1), surface chemisorbed oxygen species (O2), and surface adsorbed H_2O (O3) respectively.

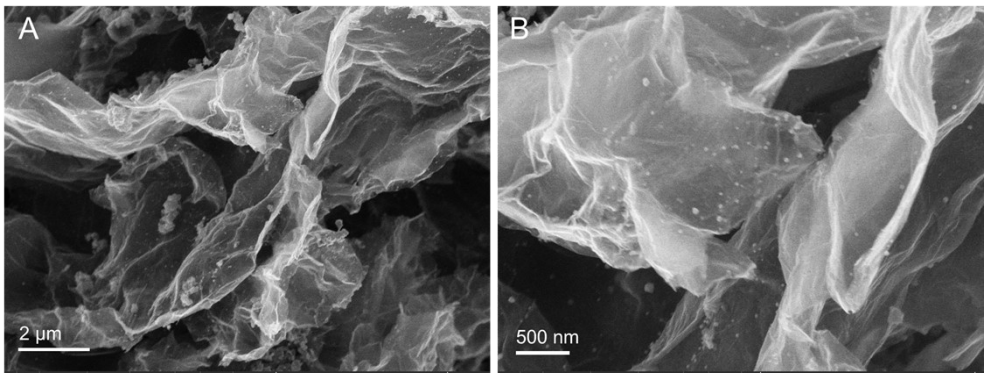

Figure S5. Morphology characterization. (A and B) SEM images for Co@Tb_2O_3/NC with different magnifications.

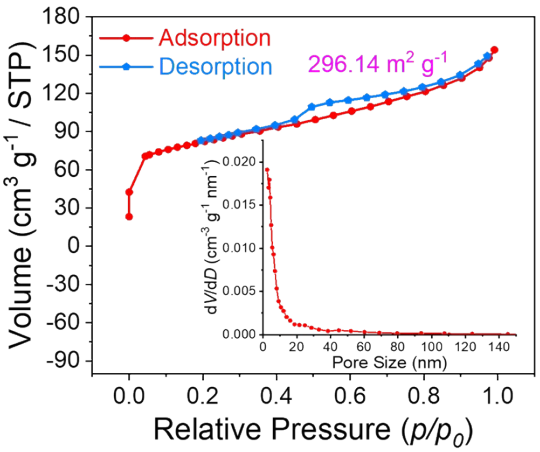

Figure S6. Surface information investigation. BET test for Co@Tb_2O_3/NC with the pore size distribution inside.

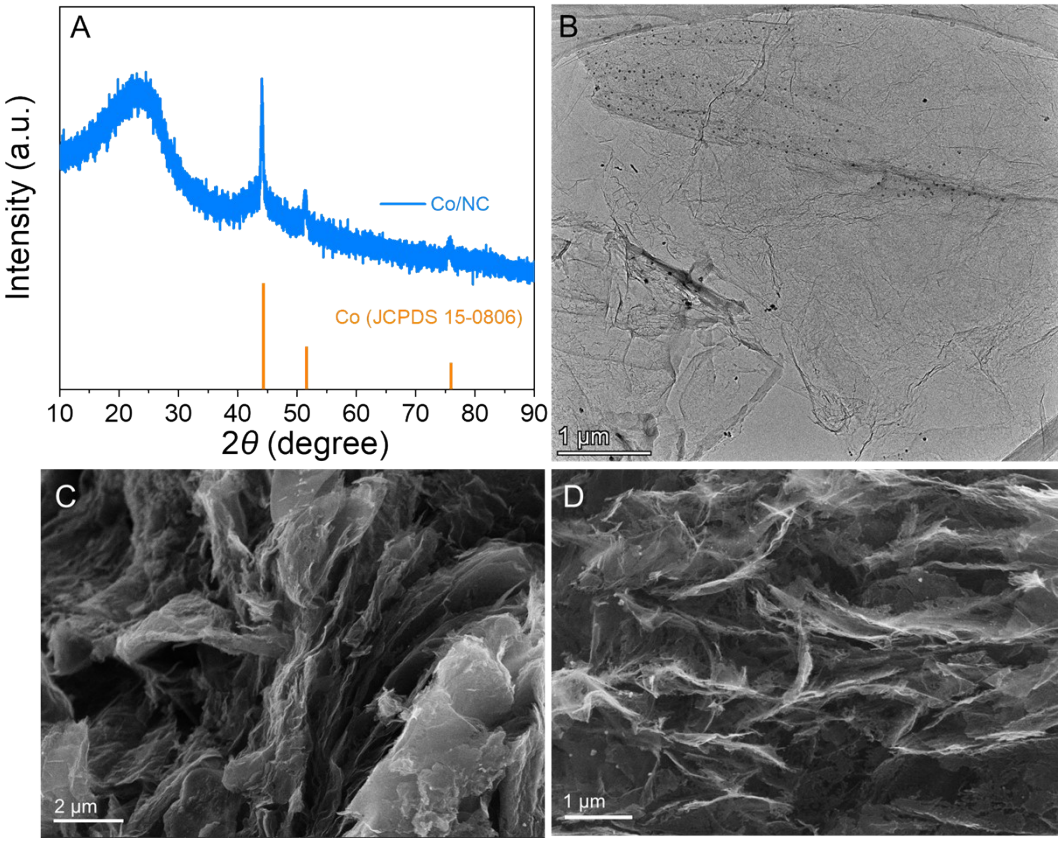

Figure S7. Physical phase determination and morphology. (A) XRD pattern of Co/NC. (B) HRTEM image for Co/NC. (C and D) SEM images for Co/NC with different magnifications.

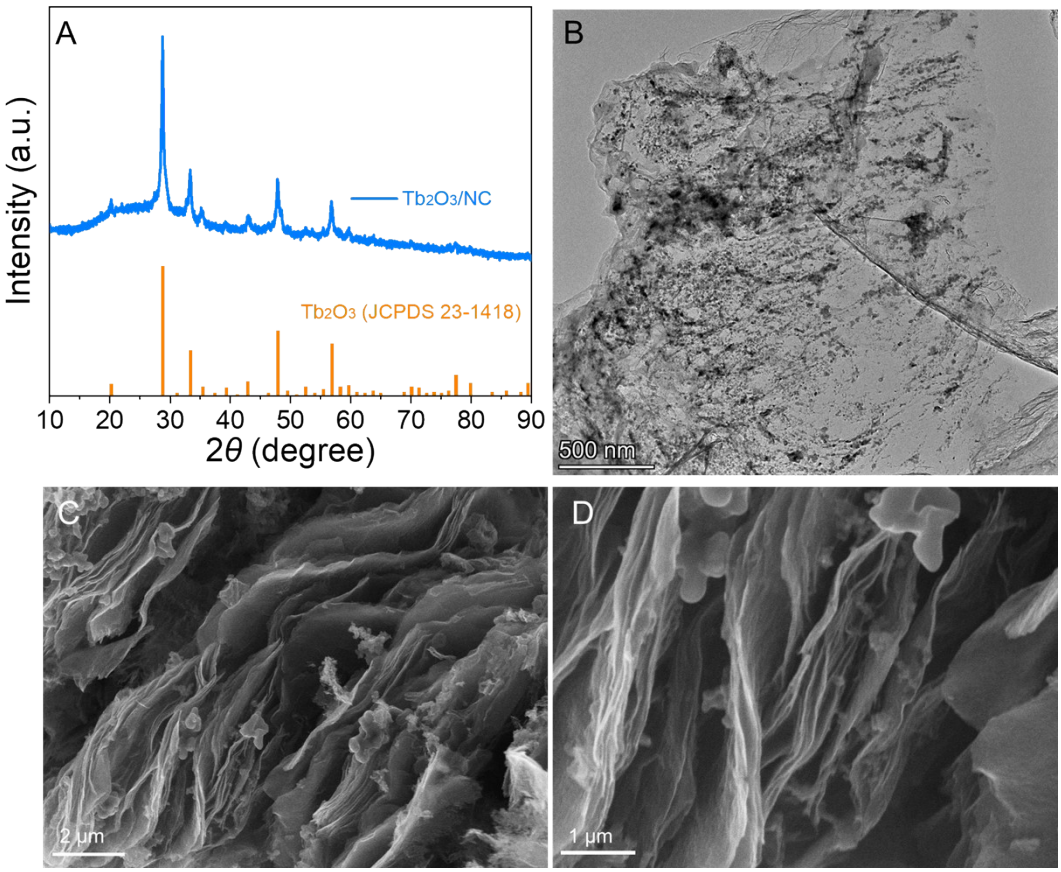

Figure S8. Physical phase determination and morphology. (A) XRD pattern of Tb_2O_3/NC. (B) HRTEM image for Tb_2O_3/NC. (C and D) SEM images for Tb_2O_3/NC with different magnifications.

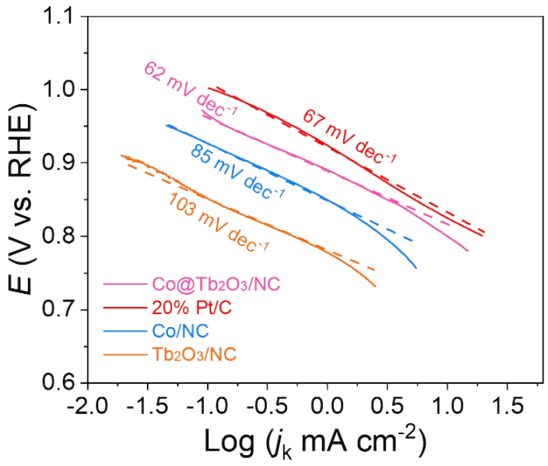

Figure S9. Kinetics analysis. Tafel plots for Co@Tb_2O_3/NC, Pt/C, Co/NC, and Tb_2O_3/NC.

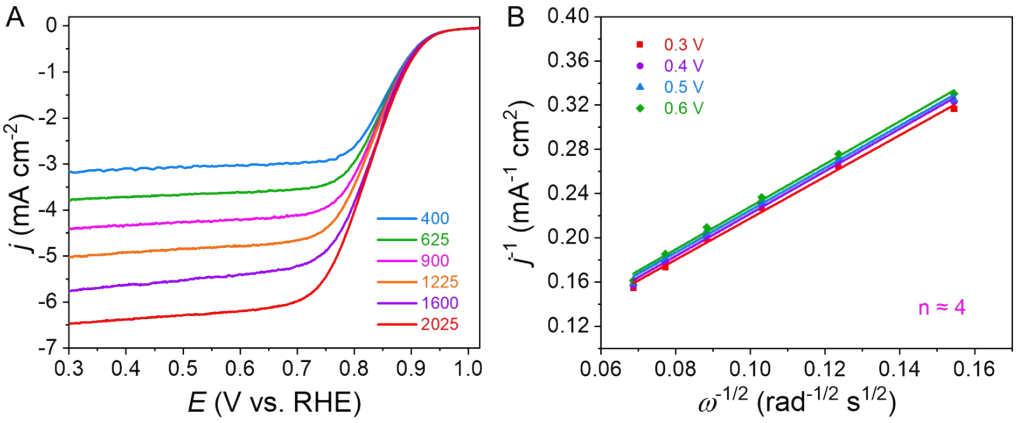

Figure S10. ORR kinetics derived from K-L analysis. (A) ORR polarization curves of catalysts with the rotating speed from 400 rpm to 2025 rpm. (B) The linearity simulation from K-L plots for *n* value.

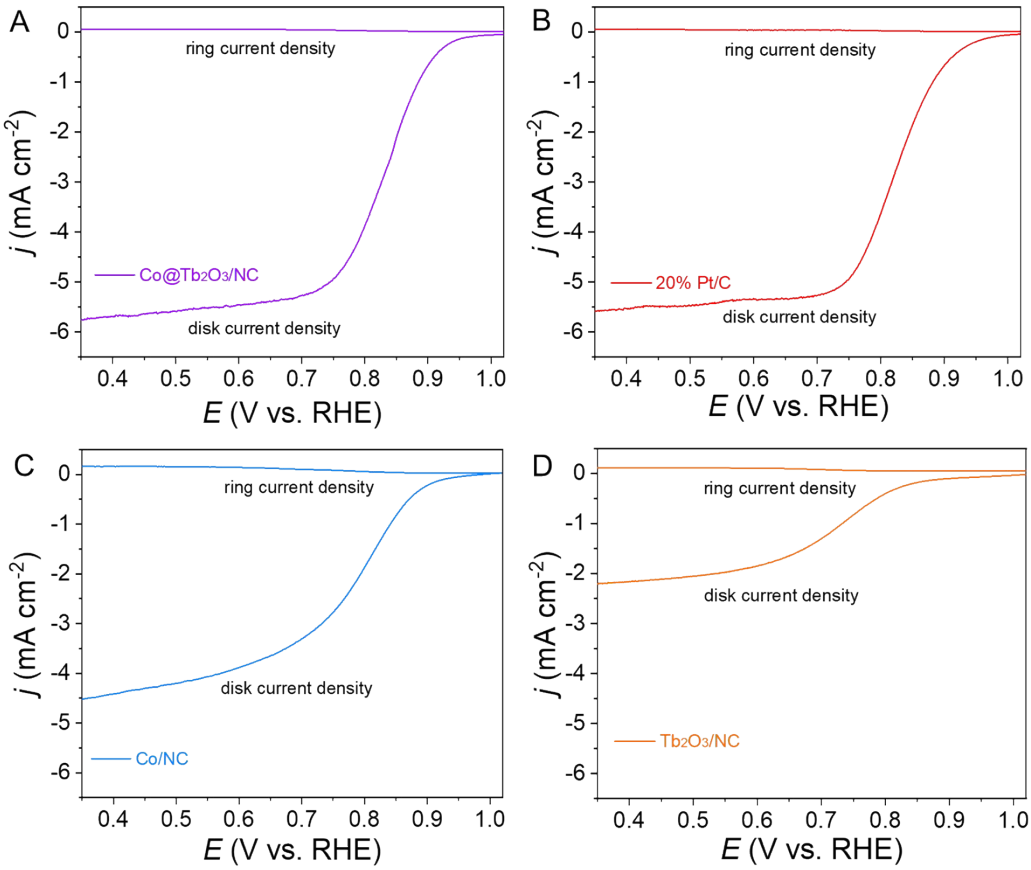

Figure S11. ORR mechanism determined by RRDE method. (A to D) RRDE tests by capturing both the disk current densities and ring current densities for Co@Tb_2O_3/NC, Pt/C, Co/NC, and Tb_2O_3/NC.

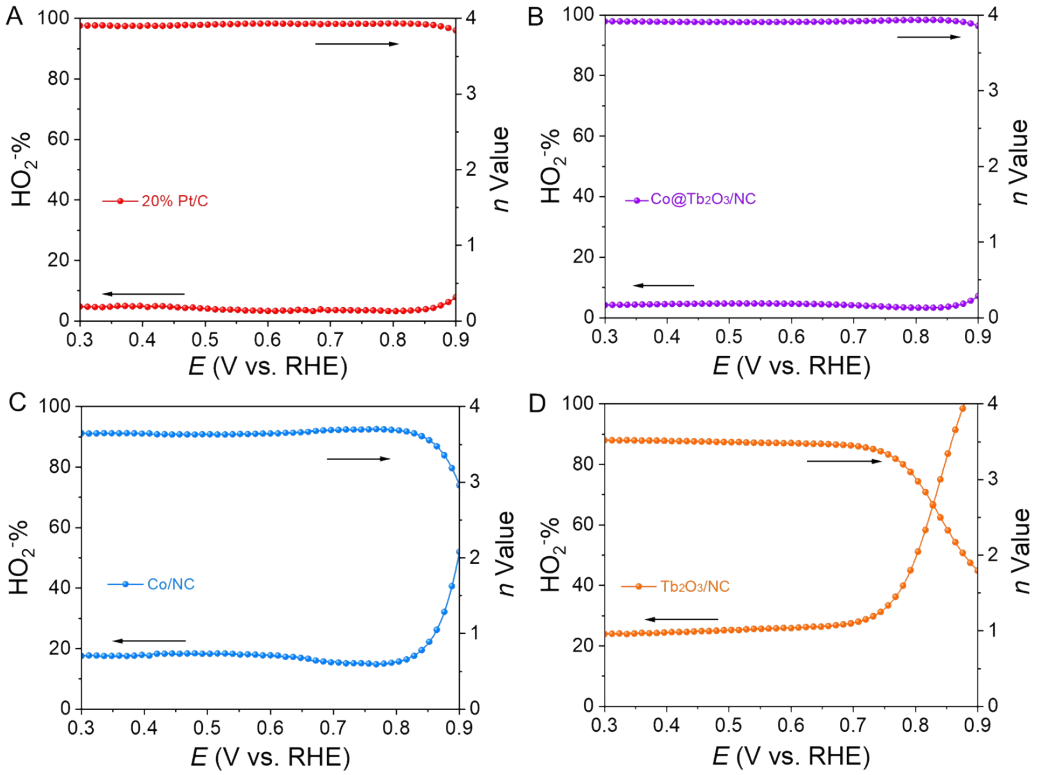

Figure S12. Determination of HO_2^- % and n value. (A to D) The calculated dynamic HO_2^- % and n value for Pt/C, Co@Tb_2O_3/NC, Co/NC, Tb_2O_3/NC.

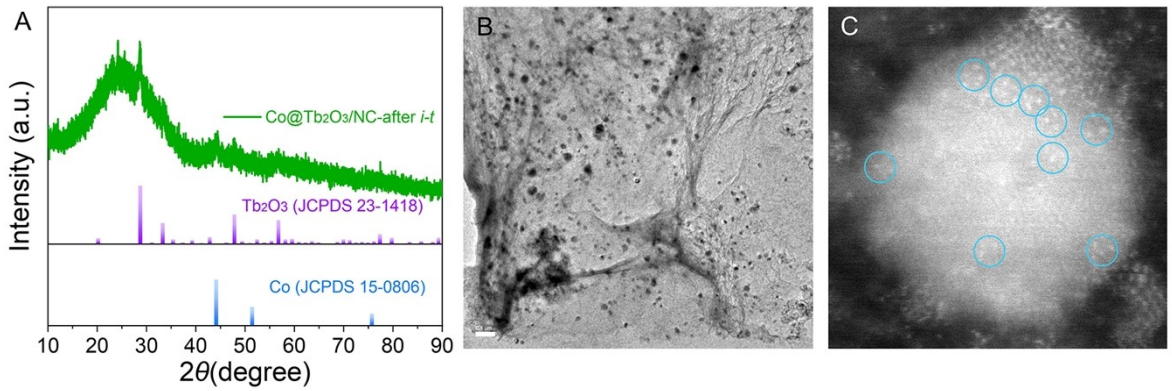

Figure S13. Characterizations after electrochemical tests. (A) XRD pattern for Co@Tb_2O_3/NC after durability test. (B) HRTEM image for Co@Tb_2O_3/NC after durability test. (C) AC-HAADF-STEM image of the recovered Co@Tb_2O_3/NC after the chronoamperometric test.

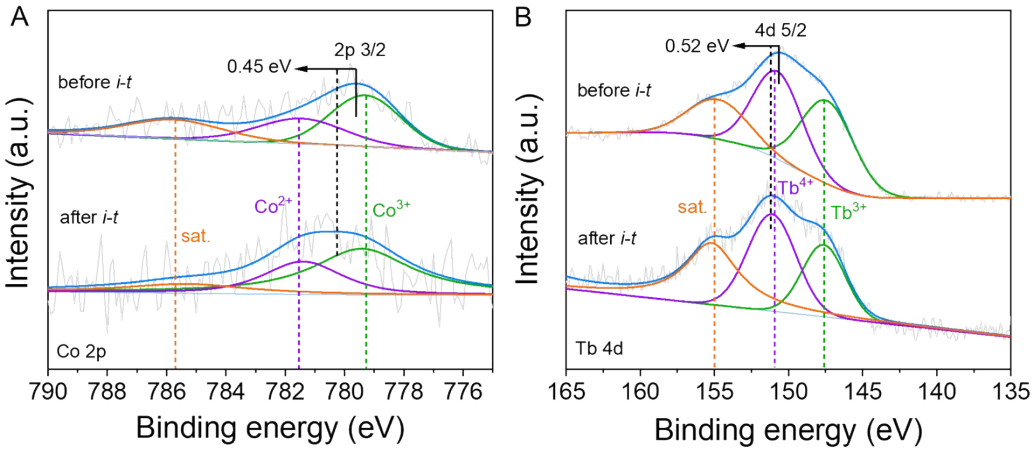

Figure S14. XPS investigation after electrochemical tests. (A-B) Comparison of high-resolution XPS spectra for Co 2*p* and Tb 4*d* in Co@Tb_2O_3/NC before and after *i-t* test.

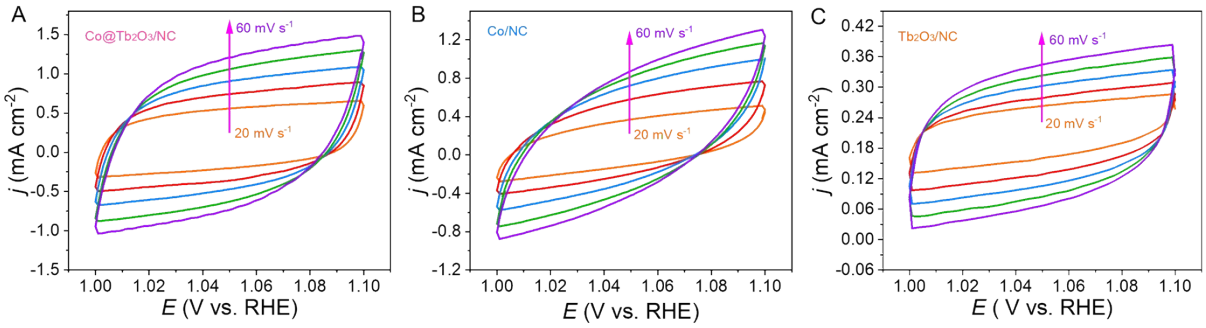

Figure S15. Double-layer capacitance tests. (A to C) CV curves in non-Faradaic potential window for Co@Tb_2O_3/NC, Co/NC, and Tb_2O_3/NC. The scanning rates shift from 20 mV s^{-1} to 60 mV s^{-1}.

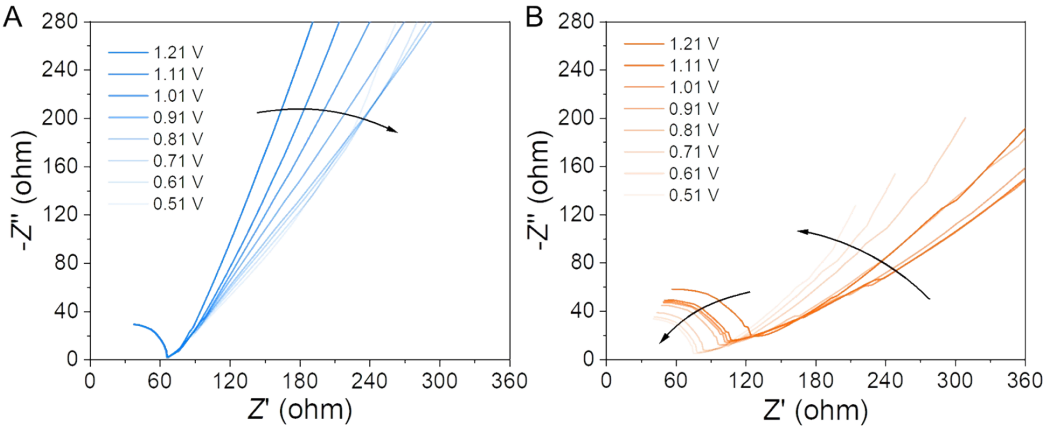

Figure S16. Potential-dependent EIS curves. (A and B) The potential-dependent EIS tests for Co/NC and Tb_2O_3/NC by shifting from 1.21 V to 0.51 V vs. RHE.

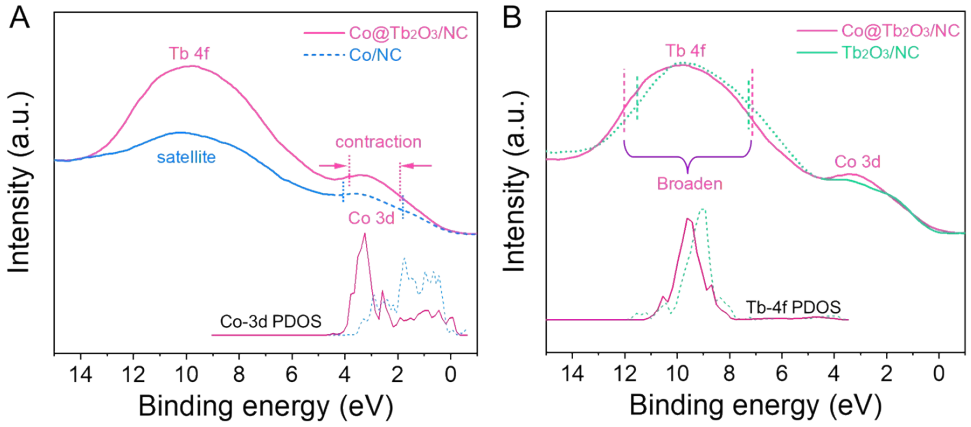

Figure S17. Consistence between experimental VB-XPS spectra and calculated PDOS. (A and B) The matching between XPS valence spectra and PDOS for Co-3d and Tb-4f.

The rationality of our electronic structure investigation can be confirmed by the comparison between the projected density of states (PDOS) and experimental valence photoemission spectra (Figure S17), where the contraction property of Co 3*d* state and the broadening of Tb 4*f* state with its band position shift are highly consistent with experimental spectra results.

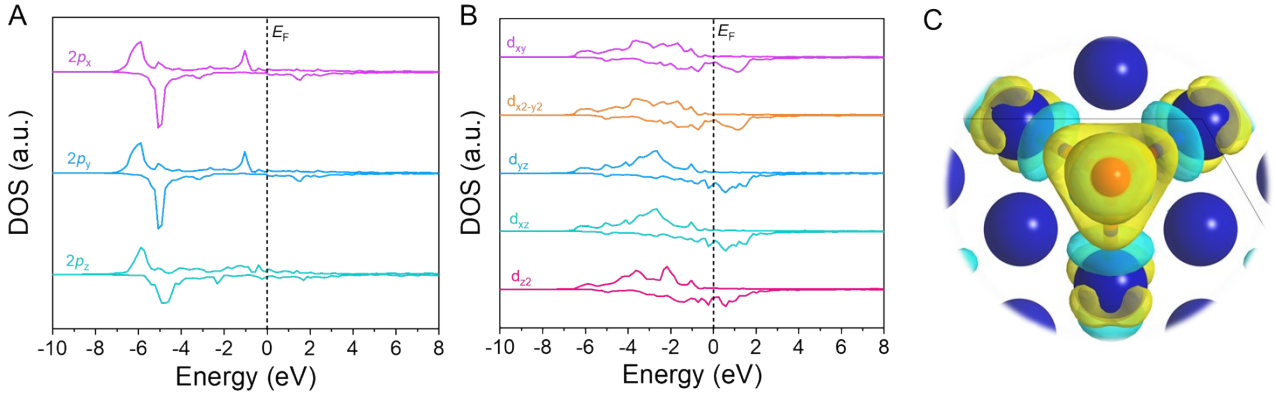

Figure S18. Calculated PDOS with corresponding charge-density difference. (A and B) The orbital-projected PDOS of *O with surface Co sites on metallic Co. (C) The charge density difference after the adsorption of *O on metallic Co.

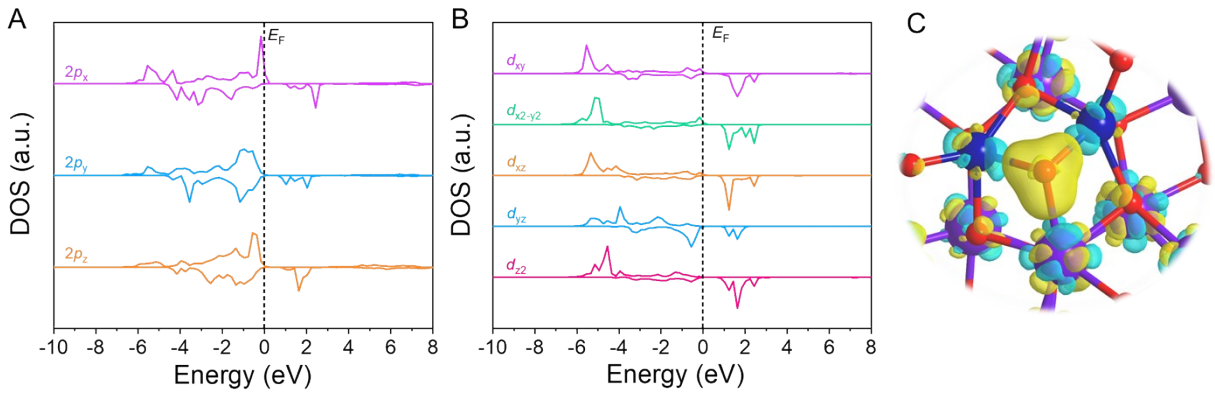

Figure S19. Calculated PDOS with corresponding charge-density difference. (A and B) The orbital-projected PDOS of *O at [Co-O-Tb] unit site in Co@Tb_2O_3 with atomic Co sites. (C) The charge density difference after the adsorption of *O on Co@Tb_2O_3.

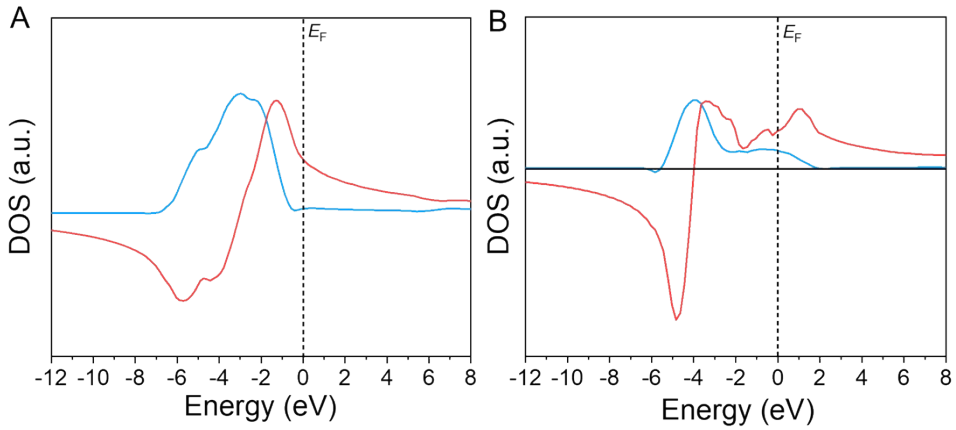

Figure S20. Signal transform for calculated PDOS. (A and B) The Hilbert transform of Co-3d PDOS for metallic Co and atomic Co sites in Co-O-Tb unit site in Co@Tb_2O_3. The blue curve is PDOS, and the red line is the Hilbert transform curve for the PDOS.

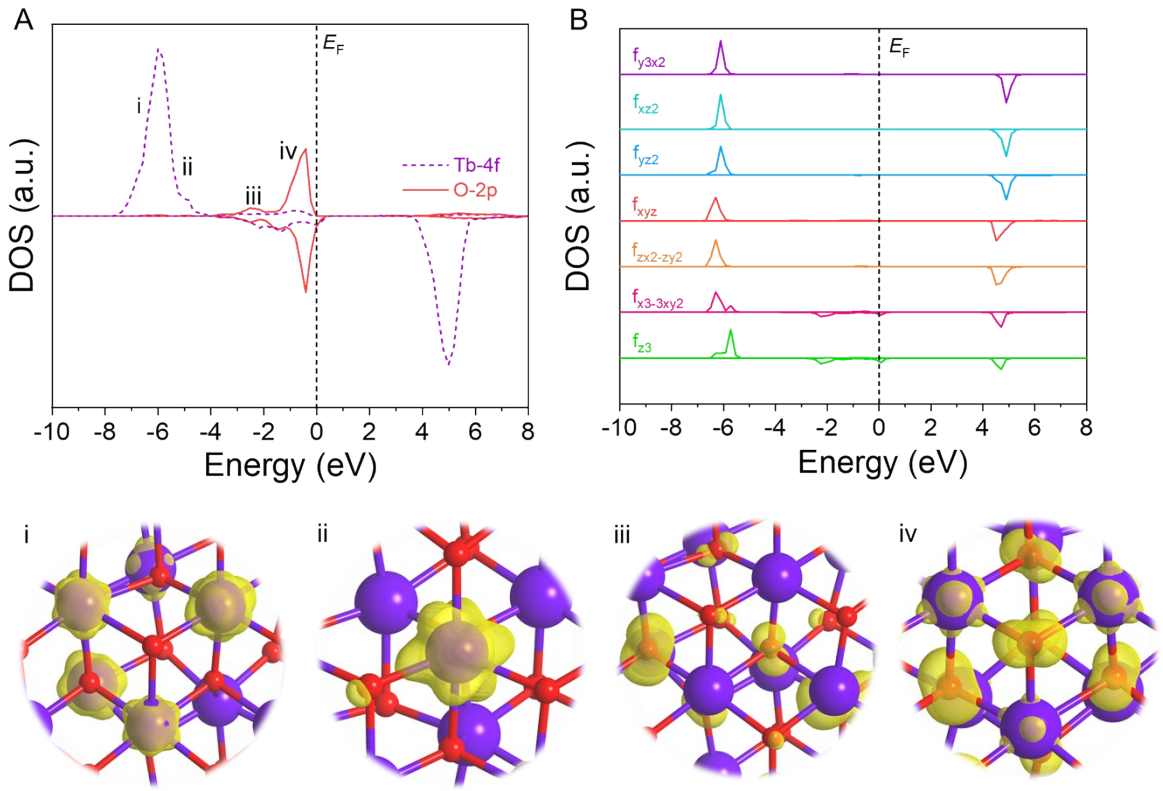

Figure S21. Electronic structure analysis aided by orbital phase. (A) The PDOS of surface Tb-4f states and O-2p states in Tb_2O_3 slab. (B) The corresponding orbital-projected 4f states for Tb. (i) to (iv) reveal the band-decomposed charge density for the interaction between Tb and O.

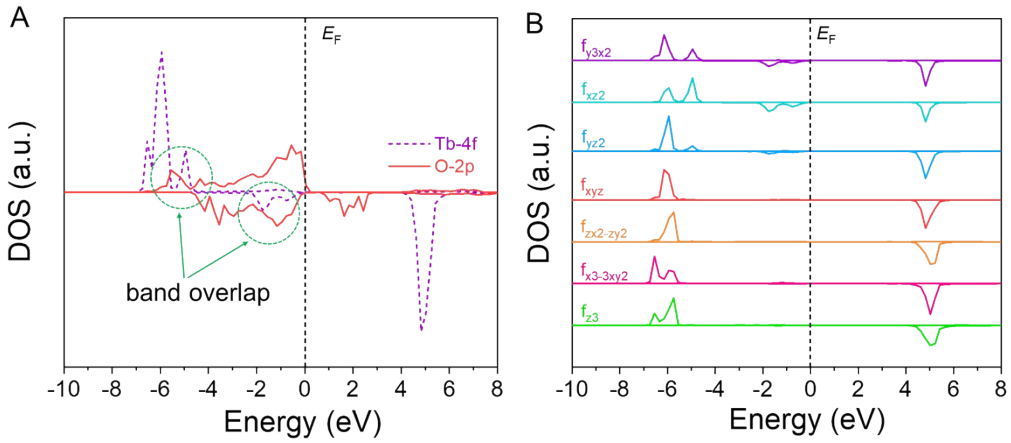

Figure S22. PDOS analysis and display. (A) PDOS of Tb-4f states in [Co-O-Tb] unit site and surface coordinated O-2p states in Co@Tb_2O_3. (B) The corresponding orbital-projected PDOS of Tb-4f states.

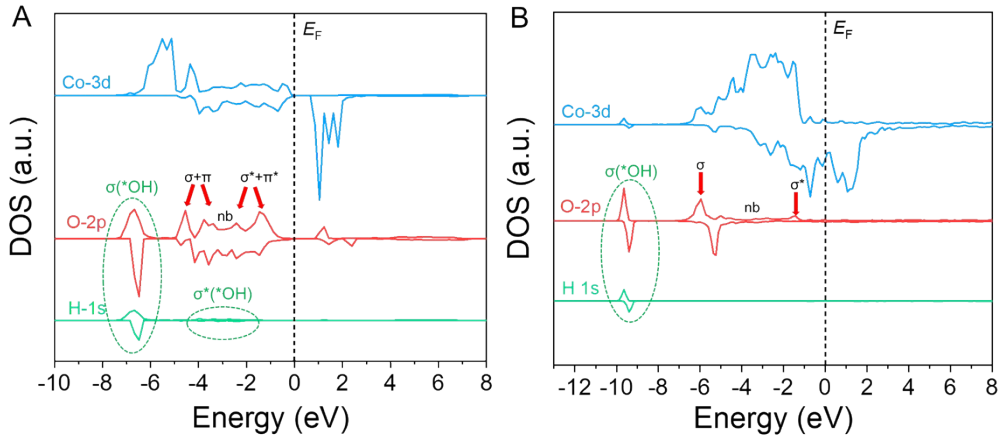

Figure S23. PDOS display for molecular orbital analysis. (A) PDOS of Co-3d at Co-O-Tb unit site in Co@Tb_2O_3 with adsorbed *OH for O-2p and H-1s states. (B) PDOS of surface Co-3d states in metallic Co with adsorbed *OH for O-2p and H-1s states.

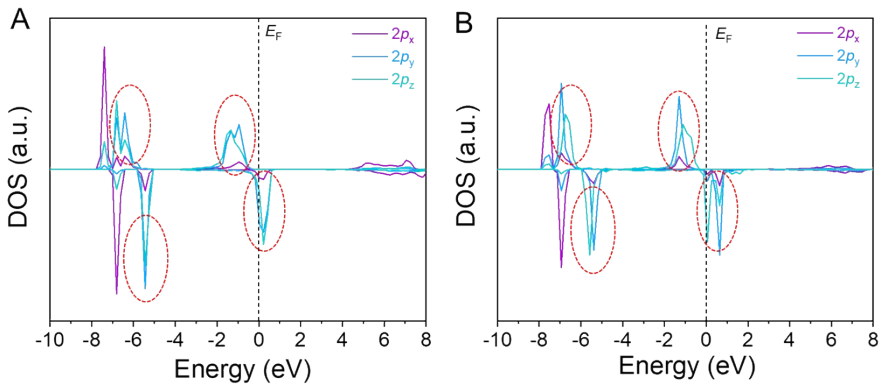

Figure S24. Determined molecular energy level for O_2. (A and B) The orbital projected PDOS of $*O_2$ at Tb_2O_3 and [Co-O-Tb] unit site in Co@Tb_2O_3.

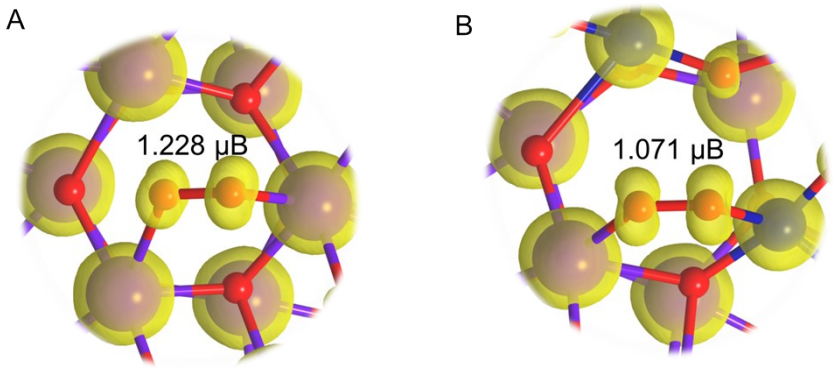

Figure S25. Spin population. (A and B) The spin density of $*O_2$ at Tb_2O_3 and [Co-O-Tb] unit site in Co@Tb_2O_3.

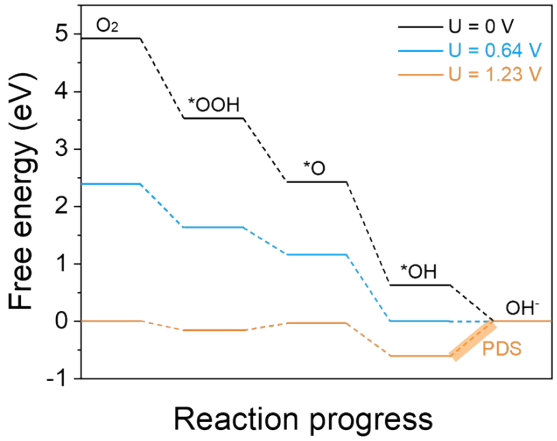

Figure S26. 4e pathway investigation. The Gibbs free energy of ORR at Tb_2O_3 under different bias potentials.

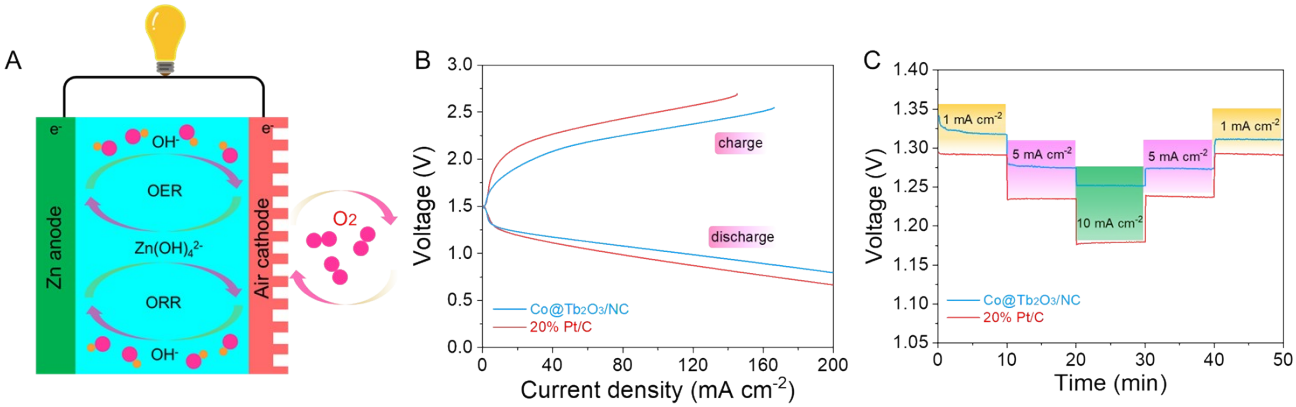

Figure S27. Basic parameters for aqueous Zn-air battery. (A) The schematic diagram of home-made flexible solid-state Zn-air battery. (B) The open-circuit potential of $Co@Tb_2O_3/NC$ and Pt/C. (C) Polarization curves for discharge and charge process.

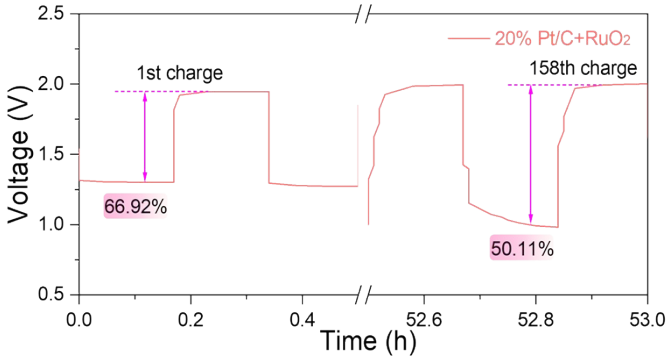

Figure S28. Long-cycle test. The voltaic efficiency of the initial and 158th charge process for Pt/C+RuO_2-based battery.

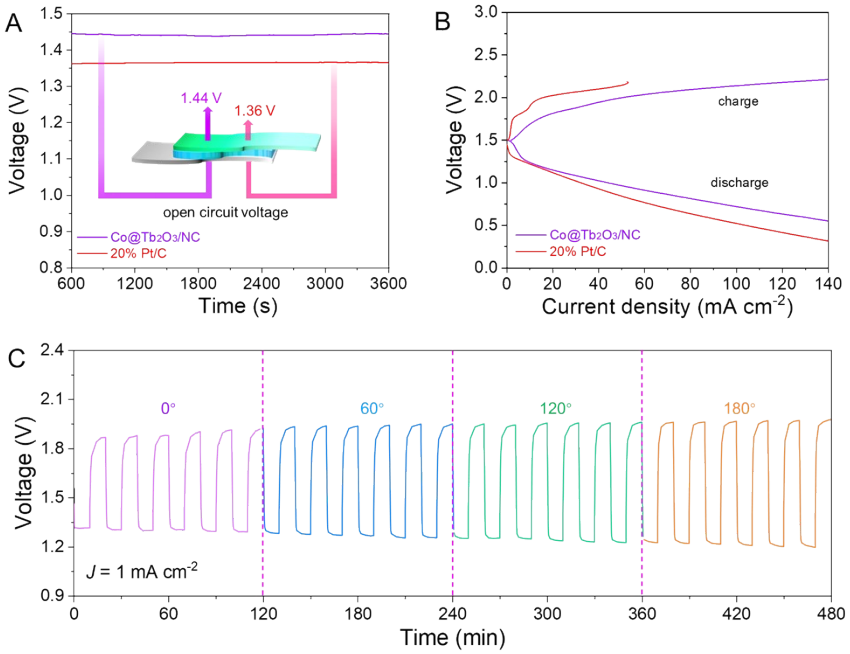

Figure S29. Basis parameters for flexible solid-state Zn-air battery. (A) The open-circuit potential for Co@Tb_2O_3/NC-based battery and Pt/C-based battery. (B) The polarization curves for discharge and charge process. (C) The flexible test under different bending angles.

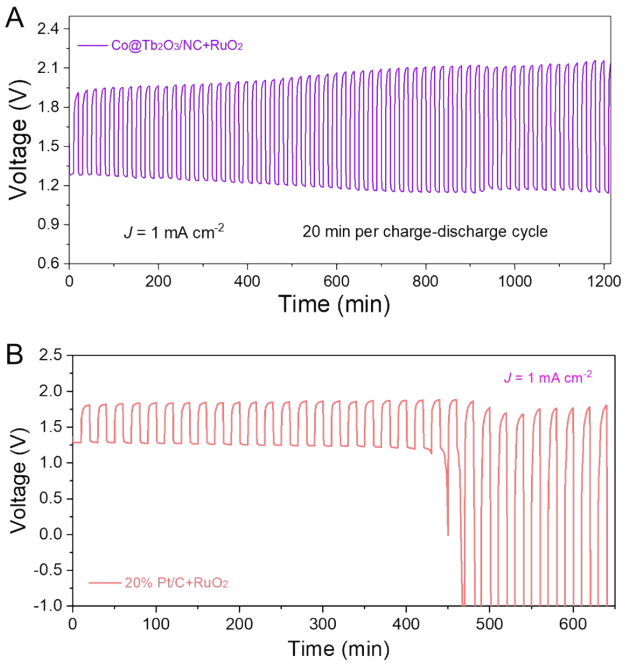

Figure S30. Long-cycle test. The long-term test with discharge and charge process under 1 mA cm^{-2} for (a) Co@Tb_2O_3/NC+RuO_2-based battery and (b) Pt/C+RuO_2-based battery.

Table S1. Comparison of the E_{onset} and $E_{1/2}$ of this work with parallel reported works.

Sample	Electrolyte	E_{onset} (V vs. RHE)	$E_{1/2}$ (V vs. RHE)	Ref.
Co@Tb_2O_3/NC	0.1 M KOH	1.02	0.85	This work
Co@NCNTs-800	0.1 M KOH	0.94	0.84	[12]
Co_3HITP_2	0.1 M KOH	0.91	0.80	[13]
PloyCoTAC	0.1 M KOH	0.928	0.832	[14]
l-CCNTs-Co-800	0.1 M KOH	0.90	0.84	[15]
A-Co@CMK-3-D	0.1 M KOH	0.946	0.835	[16]
CoS NWs@NSC-2	0.1 M KOH	0.93	0.84	[17]
Cu-14-Co_3Se_4/GC	0.1 M KOH	0.892	0.782	[18]
N-CoS_2 YSSs	0.1 M KOH	0.95	0.81	[19]
CoFe/N-GCT	0.1 M KOH	0.91	0.79	[20]
Co_3O_{4-x}	0.1 M KOH	0.98	0.84	[21]
CoNi-SAs/NC	0.1 M KOH	0.88	0.76	[22]
Co_3O_{4-x}/NG	0.1 M KOH	0.96	0.84	[23]
Gd_2O_3–Co/NG	0.1 M KOH	0.93	0.82	[24]
In-CoO/CoP FNS	0.1 M KOH	0.94	0.81	[25]
NiCoOS	0.1 M KOH	0.88	0.79	[26]
GO-Zn/Co (1:2)-800	0.1 M KOH	0.88	0.81	[27]
CoSA/N-HCS	0.1 M KOH	0.92	0.81	[28]
Co_3O_4-NP/N-rGO	0.1 M KOH	0.89	0.76	[29]
$Cu_{6.81}$-CoF	0.1 M KOH	0.91	0.80	[30]
PdNiMnO-PF	0.1 M KOH	0.94	0.84	[31]

Table S2. Comparison of the power density in aqueous Zn-air battery test.

Sample	Electrolyte	Power density (mW cm^{-2})	Ref.
Co@Tb_2O_3/NC	6 M KOH+0.2 M $ZnCl_2$	166	This work
CoN_4/NG	6 M KOH+0.2 M ZnO	115	[32]
CAN-Pc(Co)-p	6 M KOH+0.2 M $Zn(Ac)_2$	136.6	[33]
N-CoS_2 YSSs	6 M KOH+0.2 M $Zn(Ac)_2$	81	[19]
P–Co_3O_4-60 NWs	6 M KOH+0.2 M $Zn(Ac)_2$	72.1	[34]
Co/Co_3O_4@PGS	6 M KOH+0.2 M $Zn(Ac)_2$	118.7	[35]
Co-SAs@NC	6 M KOH+0.2 M $ZnCl_2$	105.3	[36]
Co_3HITP_2	6 M KOH+0.2 M $Zn(Ac)_2$	164	[13]
Gd_2O_3–Co/NG	6 M KOH+0.2 M $ZnCl_2$	114.3	[24]
A-Co@CMK-3-D	6 M KOH+0.2 M $Zn(Ac)_2$	162	[16]
Co-POC	6 M KOH+0.2 M $Zn(Ac)_2$	78.0	[37]
O–Co–N/C	6 M KOH+0.2 M $Zn(Ac)_2$	143	[38]
KJ-Co-H	6 M KOH+0.2 M $Zn(Ac)_2$	135	[39]
CoB–N_x-1:2:40-70	6 M KOH+0.2 M $ZnCl_2$	130.9	[40]
Co SA/NCFs	6 M KOH+0.2 M $Zn(Ac)_2$	154.5	[41]
Co/Co–N–C	6 M KOH+0.1 M $Zn(Ac)_2$	132	[42]
SA-PtCoF	6 M KOH+0.2 M $Zn(Ac)_2$	125	[43]

References

1. G. Kresse and J. Furthmüller, *Physical Review B*, 1996, **54**, 11169-11186.

2. G. Kresse and J. Furthmüller, *Computational Materials Science*, 1996, **6**, 15-50.

3. J. P. Perdew, K. Burke and M. Ernzerhof, *Physical Review Letters*, 1996, **77**, 3865-3868.

4. G. Kresse and D. Joubert, *Physical Review B*, 1999, **59**, 1758-1775.

5. H. J. Monkhorst and J. D. Pack, *Physical Review B*, 1976, **13**, 5188-5192.

6. S. Grimme, J. Antony, S. Ehrlich and H. Krieg, *The Journal of Chemical Physics*, 2010, **132**, 154104.

7. S. Grimme, S. Ehrlich and L. Goerigk, *Journal of Computational Chemistry*, 2011, **32**, 1456-1465.

8. S. L. Dudarev, G. A. Botton, S. Y. Savrasov, C. J. Humphreys and A. P. Sutton, *Physical Review B*, 1998, **57**, 1505-1509.

9. A. Walsh, S.-H. Wei, Y. Yan, M. M. Al-Jassim, J. A. Turner, M. Woodhouse and B. A. Parkinson, *Physical Review B*, 2007, **76**, 165119.

10. F. Ye, Z. Morgan, W. Tian, S. Chi, X. Wang, M. E. Manley, D. Parker, M. A. Khan, J. F. Mitchell and R. Fishman, *Physical Review B*, 2021, **103**, 184413.

11. J. K. Nørskov, J. Rossmeisl, A. Logadottir, L. Lindqvist, J. R. Kitchin, T. Bligaard and H. Jónsson, *The Journal of Physical Chemistry B*, 2004, **108**, 17886-17892.

12. Q. Wang, K. Ye, L. Xu, W. Hu, Y. Lei, Y. Zhang, Y. Chen, K. Zhou, J. Jiang, J. M. Basset, D. Wang and Y. Li, *Chemical Communications*, 2019, **55**, 14801-14804.

13. Y. Lian, W. Yang, C. Zhang, H. Sun, Z. Deng, W. Xu, L. Song, Z. Ouyang, Z. Wang, J. Guo and Y. Peng, *Angewandte Chemie International Edition*, 2020, **59**, 286-294.

14. A. Friedman, L. Landau, S. Gonen, Z. Gross and L. Elbaz, *ACS Catalysis*, 2018, **8**, 5024-5031.

15. Z. Liang, X. Fan, H. Lei, J. Qi, Y. Li, J. Gao, M. Huo, H. Yuan, W. Zhang, H. Lin, H. Zheng and R. Cao, *Angewandte Chemie International Edition*, 2018, **57**, 13187-13191.

16. X. Lyu, G. Li, X. Chen, B. Shi, J. Liu, L. Zhuang and Y. Jia, *Small Methods*, 2019, **3**, 1800450.

17. C. Han, Q. Li, D. Wang, Q. Lu, Z. Xing and X. Yang, *Small*, 2018, **14**, 1703642.

18. J. Dai, D. Zhao, W. Sun, X. Zhu, L.-J. Ma, Z. Wu, C. Yang, Z. Cui, L. Li and S. Chen, *ACS Catalysis*, 2019, **9**, 10761-10772.

19. X. F. Lu, S. L. Zhang, E. Shangguan, P. Zhang, S. Gao and X. W. Lou, *Advanced Science*, 2020, **7**, 2001178.

20. X. Liu, L. Wang, P. Yu, C. Tian, F. Sun, J. Ma, W. Li and H. Fu, *Angewandte Chemie International Edition*, 2018, **57**, 16166-16170.

21. L. Ma, S. Chen, Z. Pei, H. Li, Z. Wang, Z. Liu, Z. Tang, J. A. Zapien and C. Zhi, *ACS Nano*, 2018, **12**, 8597-8605.

22. X. Han, X. Ling, D. Yu, D. Xie, L. Li, S. Peng, C. Zhong, N. Zhao, Y. Deng and W. Hu, *Advanced Materials*, 2019, **31**, 1905622.

23. J. Qin, Z. Liu, D. Wu and J. Yang, *Applied Catalysis B: Environmental*, 2020, **278**, 119300.

24. M. Li, Y. Wang, Y. Zheng, G. Fu, D. Sun, Y. Li, Y. Tang and T. Ma, *Advanced Energy Materials*, 2020, **10**, 1903833.

25. W. Jin, J. Chen, B. Liu, J. Hu, Z. Wu, W. Cai and G. Fu, *Small*, 2019, **15**, 1904210.

26. Z. Bai, S. Li, J. Fu, Q. Zhang, F. Chang, L. Yang, J. Lu and Z. Chen, *Nano Energy*, 2019, **58**, 680-686.

27. W. Yang, G. Chata, Y. Zhang, Y. Peng, J. E. Lu, N. Wang, R. Mercado, J. Li and S. Chen, *Nano Energy*, 2019, **57**, 811-819.

28. Z. Zhang, X. Zhao, S. Xi, L. Zhang, Z. Chen, Z. Zeng, M. Huang, H. Yang, B. Liu, S. J. Pennycook and P. Chen, *Advanced Energy Materials*, 2020, **10**, 2002896.

29. X. Han, G. He, Y. He, J. Zhang, X. Zheng, L. Li, C. Zhong, W. Hu, Y. Deng and T.-Y. Ma, *Advanced Energy Materials*, 2018, **8**, 1702222.

30. Z. Li, Q. Wang, X. Bai, M. Wang, Z. Yang, Y. Du, G. E. Sterbinsky, D. Wu, Z. Yang, H. Tian, F. Pan, M. Gu, Y. Liu, Z. Feng and Y. Yang, *Energy & Environmental Science*, 2021, **14**, 5035-5043.

31. W. Zhang, J. Chang, G. Wang, Z. Li, M. Wang, Y. Zhu, B. Li, H. Zhou, G. Wang, M. Gu, Z. Feng and Y. Yang, *Energy & Environmental Science*, 2022, **15**, 1573-1584.

32. L. Yang, L. Shi, D. Wang, Y. Lv and D. Cao, *Nano Energy*, 2018, **50**, 691-698.

33. S. Yang, Y. Yu, M. Dou, Z. Zhang and F. Wang, *Journal of the American Chemical Society*, 2020, **142**, 17524-17530.

34. B. Tang, J. Yang, Z. Kou, L. Xu, H. L. Seng, Y. Xie, A. D. Handoko, X. Liu, Z. W. Seh, H. Kawai, H. Gong and W. Yang, *Energy Storage Materials*, 2019, **23**, 1-7.

35. Y. Jiang, Y.-P. Deng, J. Fu, D. U. Lee, R. Liang, Z. P. Cano, Y. Liu, Z. Bai, S. Hwang, L. Yang, D. Su, W. Chu and Z. Chen, *Advanced Energy Materials*, 2018, **8**, 1702900.

36. X. Han, X. Ling, Y. Wang, T. Ma, C. Zhong, W. Hu and Y. Deng, *Angewandte Chemie*

International Edition, 2019, **58**, 5359-5364.

37. B.-Q. Li, C.-X. Zhao, S. Chen, J.-N. Liu, X. Chen, L. Song and Q. Zhang, *Advanced Materials*, 2019, **31**, 1900592.

38. W. Zhang, C.-H. Xu, H. Zheng, R. Li and K. Zhou, *Advanced Functional Materials*, 2022, **32**, 2200763.

39. Z. Xing, Y.-P. Deng, S. Sy, G. Tan, A. Li, J. Li, Y. Niu, N. Li, D. Su, J. Lu and Z. Chen, *Nano Energy*, 2019, **65**, 104051.

40. V. Jose, J. M. V. Nsanzimana, H. Hu, J. Choi, X. Wang and J.-M. Lee, *Advanced Energy Materials*, 2021, **11**, 2100157.

41. Y. Han, H. Duan, C. Zhou, H. Meng, Q. Jiang, B. Wang, W. Yan and R. Zhang, *Nano Letters*, 2022, **22**, 2497-2505.

42. P. Yu, L. Wang, F. Sun, Y. Xie, X. Liu, J. Ma, X. Wang, C. Tian, J. Li and H. Fu, *Advanced Materials*, 2019, **31**, 1901666.

43. Z. Li, W. Niu, Z. Yang, N. Zaman, W. Samarakoon, M. Wang, A. Kara, M. Lucero, M. V. Vyas, H. Cao, H. Zhou, G. E. Sterbinsky, Z. Feng, Y. Du and Y. Yang, *Energy & Environmental Science*, 2020, **13**, 884-895.